MXene Supported Electrodeposition Engineering of Layer Double Hydroxide for Alkaline Zinc Batteries

Chen, Ze; Zhu, Jiaxiong; Yang, Shuo; Wei, Zhiquan; Wang, Yiqiao; Chen, Ao; Huang, Zhaodong; Zhi, Chunyi

Published in:
Angewandte Chemie - International Edition

Published: 21/10/2024

Document Version:
Final Published version, also known as Publisher's PDF, Publisher's Final version or Version of Record

Published version (DOI):
10.1002/anie.202411443

Publication details:
Chen, Z., Zhu, J., Yang, S., Wei, Z., Wang, Y., Chen, A., Huang, Z., & Zhi, C. (2024). MXene Supported Electrodeposition Engineering of Layer Double Hydroxide for Alkaline Zinc Batteries. *Angewandte Chemie - International Edition*, *63*(43), Article e202411443. https://doi.org/10.1002/anie.202411443

GDCh Research Article Angewandte International Edition Chemie www.angewandte.org

How to cite: *Angew. Chem. Int. Ed.* **2024**, *63*, e202411443
doi.org/10.1002/anie.202411443

Alkaline Zinc Batteries Hot Paper

MXene Supported Electrodeposition Engineering of Layer Double Hydroxide for Alkaline Zinc Batteries

*Ze Chen, Jiaxiong Zhu, Shuo Yang, Zhiquan Wei, Yiqiao Wang, Ao Chen, Zhaodong Huang, and Chunyi Zhi**

Abstract: The main challenges faced by aqueous rechargeable nickel-zinc batteries are their comparatively low energy density and poor cycling stability, mainly due to the limited capacity and reversibility of existing Ni-based cathodes. Moreover, the preparation procedures of these cathodes are complex and not easily scalable, which makes them less promising for large-scale energy storage. Herein, we utilized MXene as a functional additive to effectively improve the electrodeposition preparation of NiCo layered double hydroxides (LDH). Benefiting from the improved interfacial contact between nickel foam (NF) and platting solution and the enhanced ionic conductivity of platting product based on MXene additives, the resulting binder-free NiCo LDH electrode can achieve ultrahigh areal loading (~65 mg cm^{-2}) with abundant active surface for redox reactions and maintained short transport pathway for ion diffusion and charge transfer. Furthermore, the as-fabricated alkaline NiCo LDH-based battery delivers high discharge capacity, up to 20.2 mAh cm^{-2} (311 mAh g^{-1}), accompanied by remarkable rate performance (9.6 mAh cm^{-2} or 148 mAh g^{-1} at 120 mA cm^{-2}). Due to the high structural and chemical stability of MXenes/LDH-based electrode, excellent cycling life can also be achieved with 88.6 % capacity retention after 10000 cycles. In addition, ultrahigh areal energy density (31.2 mWh cm^{-2}) and gravimetric energy density (465 Wh kg^{-1}) can be simultaneously achieved. This work has inspired the design of advanced cathode materials to develop high-performance aqueous zinc batteries.

Introduction

Aqueous zinc batteries (AZBs) are attracting intensive attention benefiting from the merits of Zn anode such as high theoretical capacity (820 mAh g^{-1} or 5854 mAh cm^{-3}), low redox potential (−0.76 V vs. standard hydrogen electrode (SHE) in mild/acid electrolyte and −1.26 V vs. SHE in alkaline electrolyte), superior stability in ambient environment, and the advantage of aqueous electrolytes (intrinsic safety).[1–4] Currently, manganese- and vanadium-based oxides were the most employed cathode materials to host Zn^{2+} accompanied by the proton co-insertion or water lubrication in AZBs with mild/acid electrolyte.[5–7] These materials mainly work according to the ion-intercalation mechanism at the cathode side. In addition, organic cathodes such as quinone-based derivates and conductive polymers were recently revealed to be capable of storing Zn^{2+} due to the surface redox behaviors of accommodating Zn^{2+} at the surface heteroatoms.[8,9] Despite the merits such as low cost and nontoxicity, the relatively low specific capacities and inevitable dissolution of these cathodes during cycling still hinder the further development of AZBs.[10,11]

Alkaline Zn||Ni batteries combine high power density comparable to common supercapacitors and high discharge voltage plateau (~1.7 V) that is superior to the common AZBs with mild/acid electrolyte (normally discharge voltage < 1.5 V).[12–15] Currently, one of the fundamental bottlenecks for Zn||Ni batteries is the limited energy density, mainly arising from the low utilization of the Ni-based cathode (below 20 %).[16,17] Numerous efforts have been attempted to address this limitation, including nanoscale optimization, porous structure design, and hybrid strategies.[18,19] Various types of cathodes have been developed, such as Co_3O_4@NiO,[20] core–shell Ni@NiO,[21] phosphate ion modulation $NiCo_2O_4$,[22] and Ni/NiO heterojunction structure,[15] etc. The gravimetric capacity and lifespan have been achieved based on small active material loading (normally < 1.0 mg cm^{-2}), efficient conductive linkages, and array uniform arrangement.[17,23] However, it is known that porous nanomaterials are difficult to bond tightly together, which will essentially lead to a severe penalty in the volumetric energy density.[24,25] In addition, considering the substantial gap of their areal capacity (< 1 mAh cm^{-2}) compared to industrial-level lithium-ion batteries (above 4 mAh cm^{-2}), the developed Ni/Co-based porous nanomaterial has yet achieved practical application.[16,26] Therefore, it is necessary to explore a cost-effective way to balance the mutual

[*] Z. Chen, J. Zhu, S. Yang, Z. Wei, Y. Wang, A. Chen, C. Zhi
Department of Materials Science and Engineering, City University of Hong Kong, 83 Tat Chee Avenue, Kowloon, Hong Kong 999077, China
E-mail: cy.zhi@cityu.edu.hk
Z. Huang, C. Zhi
Hong Kong Center for Cerebro-Cardiovascular Health Engineering (COCHE), Shatin, NT, HKSAR, China

restraint between areal- and gravimetric-related specific capacities for the high active material-loaded electrodes.[27]

Transition metal-based layered double hydroxides (LDH) have emerged as attractive energy storage materials because of their decent electrical conductivity, low electronegativity, and richer redox reactions than those of the oxide counterparts and monometallic sulfides.[28,29] Herein, MXene was used as a functional additive to enhance the electrodeposition preparation of NiCo LDH effectively. By leveraging the improved interfacial contact between nickel foam (NF) and plating solution, along with the enhanced ionic conductivity of the plating product enabled by the MXene additive, an impressive ultrahigh areal loading of approximately 65 mg cm^{-2} in the NiCo LDH cathode can be achieved. Moreover, the resulting alkaline NiCo LDH-based battery exhibited outstanding performance, including remarkable discharge capacity, exceptional rate capabilities and outstanding cycling life. Furthermore, the as-fabricated battery enabled the simultaneous achievement of ultrahigh areal energy density and gravimetric energy density. These results provide valuable insights for developing advanced cathode materials in the pursuit of high-performance AZBs.

Results and Discussion

Preparation of the LDH Electrodes

The synthetic route of NiCo LDH based on the electrodeposition method is systematically described in Figure 1a. During the electrodeposition process, nitrate undergoes electrolysis with the release of OH^- on the surface of nickel foam.[30] Ni^{2+} and Co^{2+} in the solution are easy to form $NiCo(OH)_x$ precipitation with the newly generated OH^- on the surface of nickel foam. The NiCo LDH generated near the electrode substrate is readily loaded on the NF skeletons, denoted as LDH@NF. This deposition process contributes to the formation of the composite hydroxide ultrathin sheets with a porous structure. The porous structure is beneficial for fast ion transportation during the electrochemical process and reserves the active components that are not easy to peel off in the long-term cycling process.[31] Theoretically, the amount of NiCo LDH generated by electrodeposition on the surface of NF substrate would continuously increase with prolonging electrodeposition time. However, compared with the ultrathin nanosheet

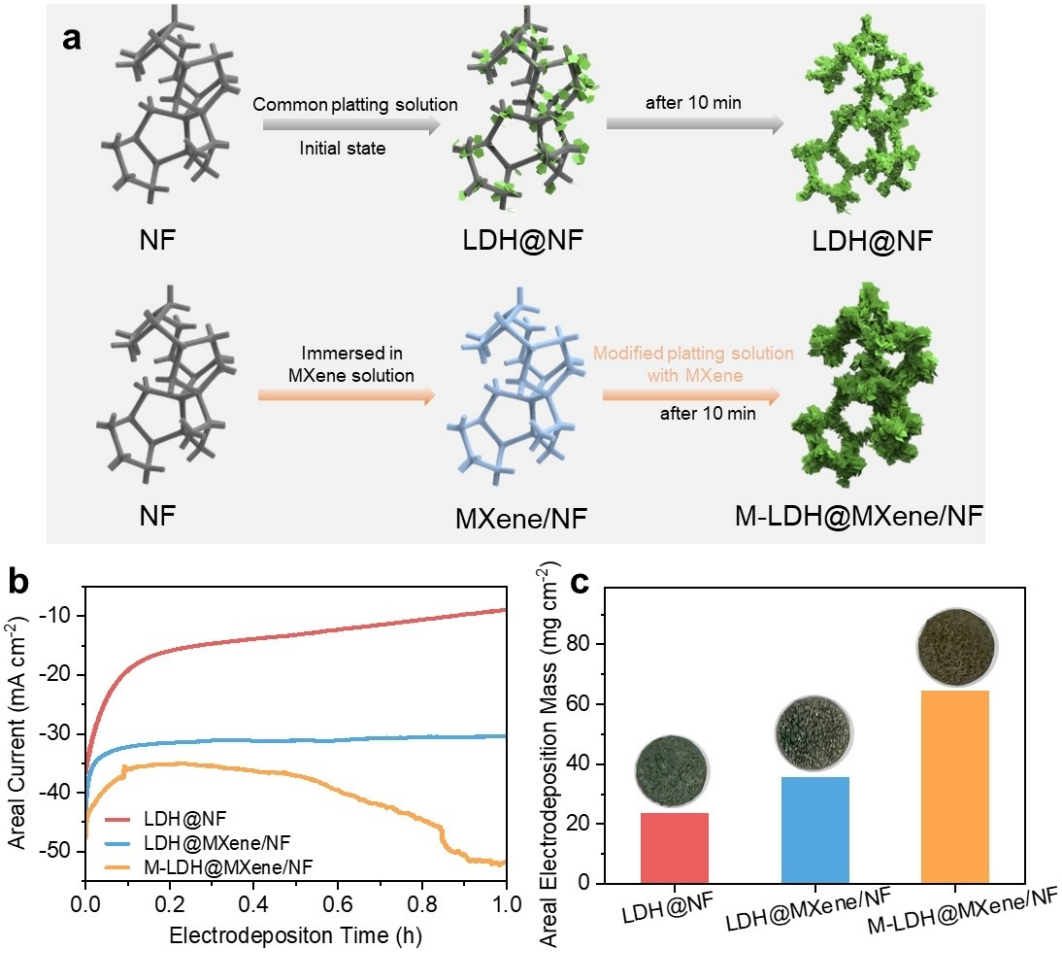

Figure 1. **Modified electrodeposition method for high-performance LDH electrodes.** a) Schematic illustration of the electrodeposition process of LDH with/without MXene additive; b) The change of response current during the electrodeposition process with time changing; c) The areal electrodeposition mass of LDH in different electrodeposition processes (inset pictures: optical pictures of the as-prepared LDH electrodes).

morphology at the initial electrodeposition process, the following electrodeposited NiCo LDH is prone to form stacked nanospheres on the surface of the initial NiCo LDH nanosheets. It can be attributed to the change in crystallization kinetic of NiCo LDH due to the inferior electronic conductivity of the LDH nanosheets and the increased OH^- concentration around the electrode surface with the dramatically decreased concentration of Co^{2+} and Ni^{2+} when prolonging the electrodeposition time.[30] To enhance the contact between LDH and NF substrate and increase the effective electrodeposited loading of LDH, MXene is selected as a highly efficient additive to support the fabrication of the NiCo LDH electrode. Firstly, $Ti_3C_2T_x$ MXene nanosheets are successfully prepared by selectively etching Al layers away from Ti_3AlC_2 and subsequently delamination under ultrasonic.[32] Scanning electron microscopy (SEM) image indicates the successful fabrication of a few-layer $Ti_3C_2T_x$ MXene (Figure S1). Owing to the electronegative characteristics, the $Ti_3C_2T_x$ MXene nanosheets could easily cover the 3D frameworks of NF (denoted as MXene/NF), leading to improved interfacial contact between NF and the platting solution due to the highly hydrophilic surface and remarkable electrical conductivity of MXene.[33] Furthermore, we also added the MXene component into the platting solution in the hope it can assist the electrodeposition of LDH based on the improved electrical conductivity of LDH, and the resulting sample is denoted as M–LDH@MXene/NF.

The electrodeposition process was carried out at a constant voltage, and the response current was recorded, as shown in Figure 1b. Compared with the preparation process of LDH@NF and LDH@MXene/NF, the response current in the electrodeposition process of M–LDH@MXene/NF is larger, indicating the enhanced electrodeposition kinetics of LDH from the synergistic effect of MXene-modified NF electrode and MXene-incorporated platting solution. Notably, the response current in the electrodeposition process of M–LDH@MXene/NF exhibits an increasing trend, which is converse to that in the fabrication process of LDH@NF and LDH@MXene/NF. During the electrodeposition process of LDH, the dispersed MXenes in the plating solution were adsorbed and incorporated into the LDH structure, enhancing the electrical conductivity and structural stability of the LDH and promoting a highly efficient electrodeposition process.[33] In addition, we also investigated the effect of electrodeposition time on the effective mass loading of LDH in the fabrication process. Compared with the 1 h electrodeposition, the increasing amount of LDH on the electrode becomes negligible when further prolonging the electrodeposition time. Thus, 1 h is the appropriate time considering the time cost (Figure S2). Furthermore, the highest areal loading mass of LDH can be achieved in the M–LDH@MXene/NF electrode, reaching ~65 $mg\,cm^{-2}$, which is much higher than LDH@NF (24 $mg\,cm^{-2}$) and LDH@MXene/NF (36 $mg\,cm^{-2}$) (Figure 1c). We have also tested the electrochemical resistance of the as-prepared electrodes at different electrodeposition times (Figure S3). As the electrodeposition process continues, the charge-transfer resistance of the LDH@NF and LDH@MXene/NF electrodes gradually increases. However, the M–LDH@MXene/NF electrodes consistently exhibit low charge-transfer resistance throughout the electrodeposition process. This indicates that the incorporated MXene effectively facilitates ion and electron transfer on the electrode surface, which is beneficial for large-loading electrodeposition of LDH. All the above results confirm the advance of MXene additive in the LDH electrodeposition process.

Morphologies of the LDH Electrodes

Subsequently, we thoroughly investigated the morphologies of the electrodeposited LDH in different electrodeposition processes. As shown in Figure S4, the surface of pure NF is relatively smooth. When pure NF was directly employed as the substrate for the electrodeposition, obvious irregular nanoparticles could be detected on the surface of NF after 20 min electrodeposition, indicating the inferior preparation of LDH nanosheets (Figure 2a). Then, MXene was adopted to modify the surface of pure NF and as shown in Figure 2b, the surface of NF after modification becomes slightly rough, suggesting the successful coating of MXene on the surface of NF. Furthermore, the modified MXene/NF was used as the substrate for the LDH preparation. In the initial 20 min electrodeposition process, the LDH nanosheets grow constantly, and the profile of LDH nanosheets on the surface of MXene/NF becomes relatively obvious, as shown in Figure S5. However, when the electrodeposition time reaches 1 h, the same irregular LDH nanoparticles appear again in the LDH@MXene/NF electrode (Figure 2c), and no LDH nanosheets can be detected even in the enlarged SEM image of the LDH@MXene/NF electrode (Figure 2d). These results indicate that merely modifying the NF with MXene is not able to promote the highly efficient electrodeposition of LDH nanosheets, especially when prolonging the electrodeposition time.

Then, we added the MXene to the platting solution to assist in the electrodeposition of LDH. As seen from Figure 2e, when the electrodeposition time increases to 1 h, the LDH nanosheets still can be observed clearly. The 3D open architecture is obtained by forming the interlaced structure with a number of honeycomb-like pores, which will provide channels for ion transportation and increase the area of interface between active sites and solution (Figure 2f).[34] The mapping images show that Ni and Co elements are uniformly distributed on the surface of the electrode, as shown in Figure 2g–j. It is worth noting that obvious Ti elements can be detected on the surface of the electrode, confirming the incorporation of MXene in the electrodeposition process (Figure 2k). The above results indicate that MXene can serve as a high-performance additive to support the electrodeposition of LDH nanosheets.

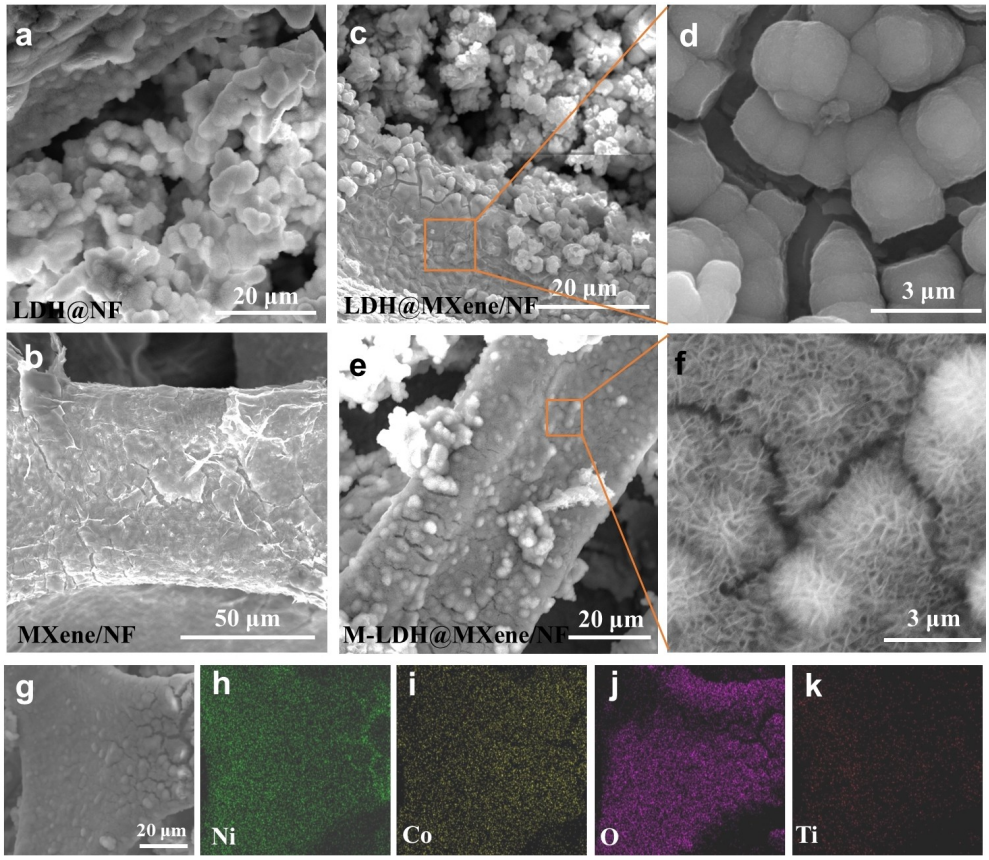

Figure 2. **Morphologies characterization of the electrodeposited LDH electrodes**. SEM images: a) LDH@NF; b) MXene/NF; c) LDH@MXene/NF and d) the enlarged view of selected area; e) M–LDH@MXene/NF and f) the enlarged view of selected area. g) The SEM image of M–LDH@MXene/NF electrode and elemental mappings of h) Ni, i) Co, j) O and k) Ti.

Structural Characterization of the LDH Electrodes

To further investigate the structure and composition of NiCo LDH nanosheets, a high-resolution transmission electron microscope (HRTEM) examination was carried out by peeling off LDH nanosheets from the M–LDH@MXene/NF electrode obtained at 1 h electrodeposition time. The HRTEM images at different magnifications are shown in Figure 3a and b. As seen in Figure 3a, the LDH nanosheets exhibit irregular two-dimensional plate shapes of around 1 m in size, which are slightly transparent in the direction of the two-dimensional plane, indicating that the LDH nanosheets prepared here are ultra-thin. We further amplified Figure 3a to obtain the HRTEM image of LDH nanosheets in-plane direction, shown in Figure 3b. It is observed that the LDH nanosheets have a polycrystalline structure with a well-organized orthohexagnal lattice fringe. The crystal lattice spacing is about 0.23 nm, which corresponds to the (1 1 0) lattice planes of NiCo LDH.[35]

Subsequently, X-ray diffraction (XRD) was adopted to disclose the crystal structure of the resultant samples. As shown in Figure 3c, the characteristic peaks located at 33.4° and 59.5° can be denoted as the NiCo LDH, which correspond well with the standard spectra of NiCo LDH (PDF # 32-1383).[36] In addition, the apparent characteristic peak of $Ti_3C_2T_x$ MXene can also be detected at 44.2° in the M–LDH@MXene/NF electrode, indicating the simultaneous deposition of MXene during the electrodeposition process.[33] In addition, X-ray photoelectron spectroscopy was also conducted to reveal further the chemical compositions and states of the as-prepared electrodes. The general XPS survey spectra of NiCo LDH-based electrodes are shown in Figure S6, verifying the co-existence of Co, Ni, Ti, C and O elements. As exhibited in Figure 3d, four characteristic peaks at 879.6, 873.2, 861.6, and 855.7 eV are observed in the Ni 2p spectrum, which corresponds to 2p1/2 and 2p3/2 doublet of Ni^{3+}.[37] In Figure 3e, the Co 2p spectrum shows four dominated peaks at 802.8, 796.8, 786.1 and 780.9 eV, ascribing to Co 2p1/2 and 2p3/2 of Ni^{3+} in NiCo LDH-based electrodes.[22] Furthermore, the Ti 2p characteristic peaks can only be detected in the M–LDH@MXene/NF electrode, confirming the incorporation of $Ti_3C_2T_x$ MXene in the electrodeposition process again.[37] The resultant Ti elements mainly exhibit Ti–C bond from $Ti_3C_2T_x$ MXene and the TiO_2 from the decomposed/oxidized $Ti_3C_2T_x$ MXene.[38] MXenes possess excellent mechanical properties, such as high tensile strength and flexibility. When incorporated into NiCo LDH materials, MXenes reinforce the overall structure, making it more resistant to mechanical stress and deformation. In addition, due to the 2D feature of MXenes,

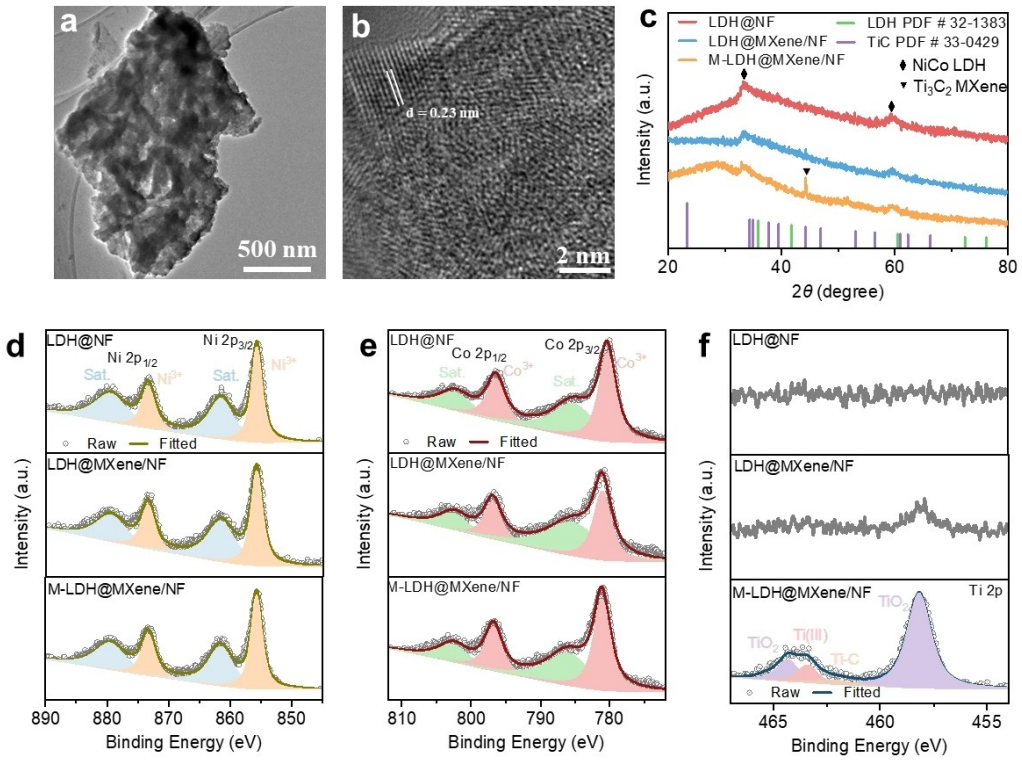

Figure 3. **Structural characterizations of NiCo LDH-based electrodes**. a) TEM image of NiCo LDH nanosheets from M–LDH@MXene/NF and b) the corresponding HRTEM image in the direction of the plane; c) XRD patterns of the three NiCo LDH-based electrodes; XPS spectra of the three NiCo LDH-based electrodes: d) Ni 2p, e) Co 2p and f) Ti 2p.

they can provide additional support and prevent the layers of LDH from collapsing or delaminating. This interlayer strengthening contributes to the durability and stability of the material.[33]

Electrochemical Performance NiCo

We initially investigated the electrochemical performance of the as-prepared NiCo LDH-based electrodes in alkaline zinc batteries. As observed from the cyclic voltammetry (CV) curves of the as-fabricated batteries, all three electrodes show one obvious anodic peak at ~1.52 V. During the subsequent cathodic scan, one cathodic peak is also detected at ~1.71 V, corresponding to their reverse process. Furthermore, the galvanostatic charge/discharge (GCD) curves of the three batteries in Figure 4b show long discharge plateaus located at ~1.61 V (LDH@NF), 1.62 V (LDH@MXene/NF) and 1.61 V (M–LDH@MXene/NF), respectively, and up to 20.2 mAh cm^{-2} areal capacity can be achieved in the M–LDH@MXene/NF electrode, which is much larger than that of LDH@NF electrode (2.06 mAh cm^{-2}) and LDH@MXene/NF electrode (8.79 mAh cm^{-2}). In addition, the specific capacities of the three electrodes are 80.5 mAh g^{-1} (LDH@NF), 253.4 mAh g^{-1} (LDH@MXene/NF) and 311.7 mAh g^{-1} (M–LDH@MXene/NF), respectively (Figure S7). The superior capacity of M–LDH@MXene/NF electrode can be attributed to the low bulk resistance and charge-transfer resistance compared with that of the other two electrodes (Figure S8). In addition, the areal capacity and specific capacity of M–LDH@MXene/NF electrode surpass most other electrode materials in alkaline zinc batteries, demonstrating the potential of the NiCo LDH with MXene in constructing high-energy cathode.[13,15,22] Furthermore, the corresponding differential capacity versus voltage plot (dQ dV^{-1}) was carried out based on the GCD curves of the three electrodes (Figure 4c). The clear, sharp decline in voltage hysteresis can be observed in the three electrodes, and there is no obvious difference in the peak voltage of the three electrodes, further confirming the result in Figure 4a.

Subsequently, the rate performance of the M–LDH@MXene/NF-based battery was assessed by the GCD curves at different current densities (Figure 4d). The same reaction plateau at around 1.6 V can be observed at all curves, meanwhile, the battery exhibits a remarkable rate capability of 20.2, 18.7, 17.6, 16.9, 15.9, 13.1 and 9.6 mAh cm^{-2} based on the mass of the electrodeposited NiCo LDH at 5, 10, 20, 40, 60, 90 and 120 mA cm^{-2}, respectively, corresponding to 311, 289, 272, 261, 245, 202 and 148 mAh g^{-1}. When suddenly shifting the current density back to 5 mA cm^{-2}, the capacity recovers to 19.7 mAh cm^{-2}, indicating a fast electrochemical redox kinetics in the as-prepared electrode (Figure 2e), which is also reflected by the low resistances of both charge transfer and Warburg diffusion of NiCo LDH nanosheets (Figure S8).[39] In addition, we also compared the rate performance of the developed M–LDH@MXene/NF-based battery with other

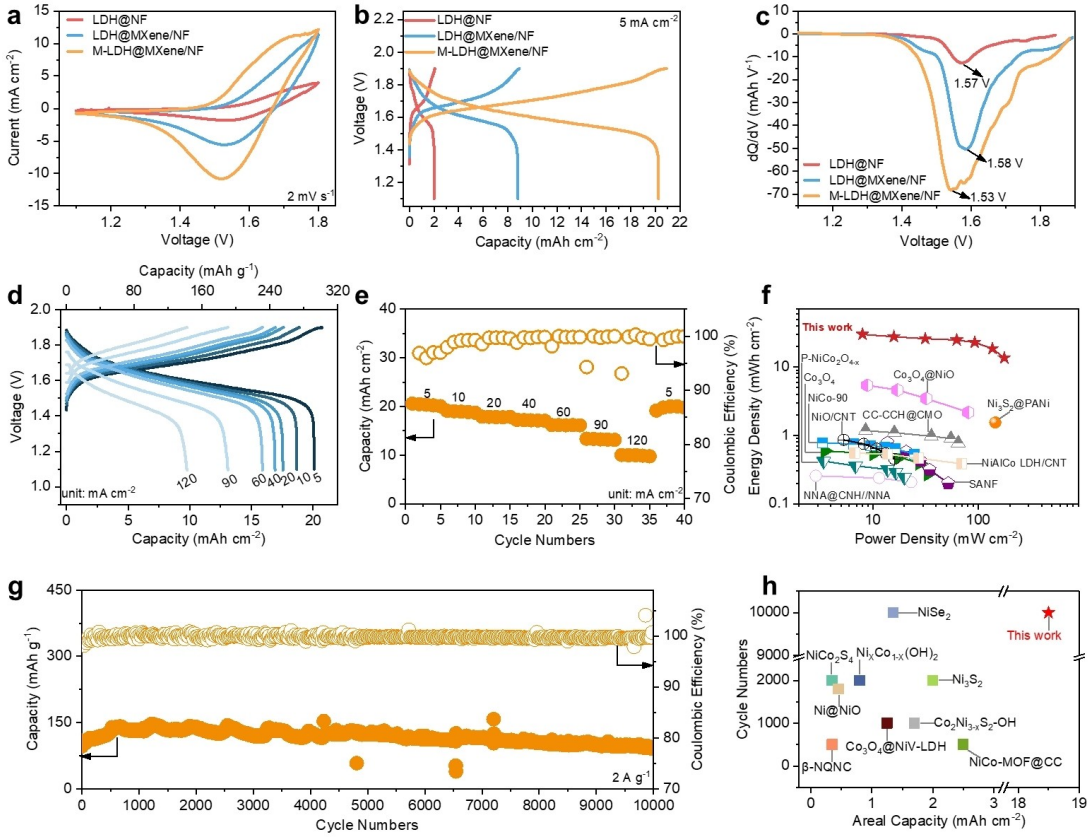

Figure 4. **Electrochemical performance of the as-prepared NiCo LDH in alkaline zinc batteries**. Alkaline zinc||NiCo battery with the three NiCo LDH electrodes: a) CV curves at 2 mV s^{-1}; b) GCD curves at 5 mA cm^{-2}; and c) the corresponding differential capacity versus voltage plot (dQ dV^{-1}). Alkaline zinc battery with M–LDH@MXene/NF electrode: d) GCD curves at different current densities and e) the corresponding rate performance; f) comparison of the areal power density and energy density between the M–LDH@MXene/NF-based battery with other reports (NiCo-MOF@CC: NiCo-metal–organic framework@current collector; β-NQNC: β-$Ni(OH)_2$ quasi-nanocubes); g) long-term cycling performance at 2 A g^{-1}; h) comparison of the areal capacity and cycling performance between the M–LDH@MXene/NF-based battery with other reports.

reports (Figure S9). The LDH-based cathode materials demonstrate significant superiority over other cathode materials for AZBs, further confirming the advantages of the modified electrodeposition method in developing high-performance LDH materials. It is worth noting that the Coulombic efficiency of the battery is as low as ~92%, which can be partly attributed to the decomposition of aqueous electrolytes.[40] In addition, the areal energy density in most reported alkaline zinc batteries is lower than 2 mWh cm^{-2}. However, in our alkaline zinc battery, due to the ultrahigh loading density and excellent electrochemical activity of the M–LDH@MXene/NF cathode, ultrahigh areal energies and power densities (31.2 mW cm^{-2} at 7.9 mW cm^{-2}, 13.5 mWh cm^{-2} at 180 mW cm^{-2}) were achieved (Figure 4f).[17,21,23,41–46] In addition, as shown in the gravimetric Ragone plots in Figure S10, both high energy and power densities (465 Wh kg^{-1} at 132 W kg^{-1} and 207 Wh kg^{-1} at 2752 W kg^{-1}) can be simultaneously achieved based on the mass of NiCo LDH. These values outperform reported alkaline Zn||Ni batteries and most developed aqueous batteries, further revealing the superiority of the developed MXene assisted LDH-based electrode (Table S1). Furthermore, long lifespan is vital for practical application of alkaline zinc batteries. As shown in Figure 4g, the M–LDH@MXene/NF battery exhibits excellent cycling performance, with a high capacity retention of 88.6% after 10000 cycles at 2 A g^{-1} and high Coulombic efficiency. High capacities of 94.7 mAh g^{-1} and 6.2 mAh cm^{-2} could be maintained. Moreover, we compared the cycling performance and areal capacity of our battery with other reports, further confirming the superiority of the M–LDH@MXene/NF electrode (Figure 4h).[17,23,40–45] Such remarkable cycling performance also can be attributed to the high electrode stability from the modified electrodeposition method, which can be confirmed by the remained LDH nanosheets morphology with porous structure after the long-term cycling (Figure S11).

Conversion Mechanism of the Alkaline Zinc Battery

To reveal the reaction mechanism of the M–LDH@MXene/NF electrode in alkaline electrolyte, we investigated the chemical structure transition behavior by ex situ Raman analysis. Figure 5a shows the GCD profiles of the charge/discharge curve of M–LDH@MXene/NF electrode in the

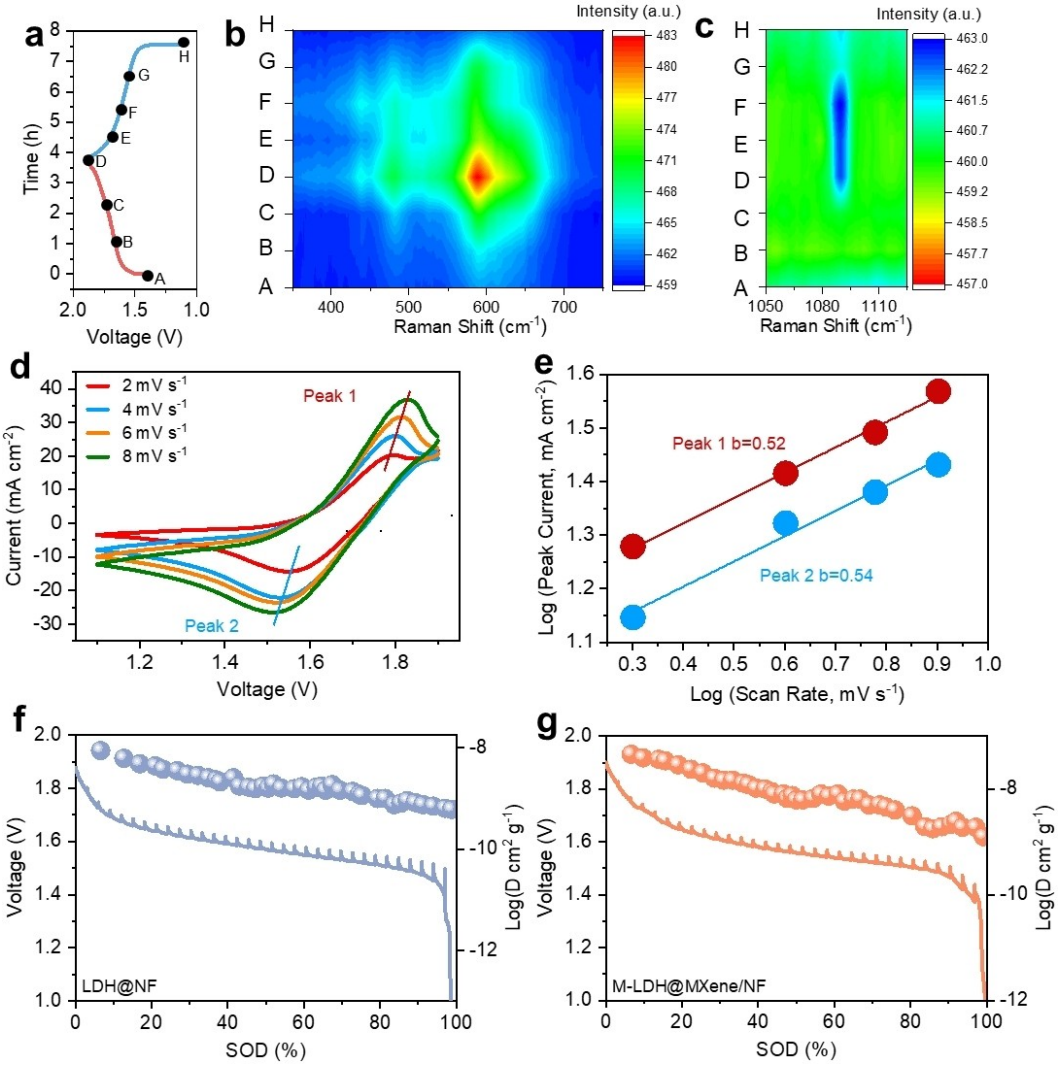

Figure 5. **Redox kinetics of the developed M–LDH@MXene/NF-based alkaline zinc battery**. a) The GCD curve of alkaline zinc battery at 5 mA cm^{-2}; b) and c) ex situ Raman spectra at selected potentials as marked in Figure 5a; d) CV curves with scan rates ranging from 2 to 8 mV s^{-1}; e) the relationship between log (peak current) and log (scan rate); GITT profiles (10 mA cm^{-2} for 60 s followed by a 0.5 h rest) with the corresponding ion diffusivity during the discharge process: f) LDH@NF-based battery and g) M–LDH@MXene/NF-based battery.

alkaline zinc battery. When the LDH-based electrode was charged to 1.6 V, two new peaks emerged at ~482 and 584 cm^{-1}, which can be ascribed to the characteristic peaks of M^{III}–O (M: Ni, Co) (Figure 5b).[47,48] With the charge process proceeding, the characteristic peaks of M^{III}–O show slightly enhancement in strength, and when the LDH-based electrode was discharged to 1.1 V, the characteristic peaks of M^{III}–O totally disappear, which reveals a clear transition between Ni^{2+} to Ni^{3+}. In addition, as shown in Figure 5c, during the charging process, the characteristic peak of MOO^{-} (M: Ni, Co) located at 1089 cm^{-1} gradually appears, and during the subsequent discharging process, the peak gradually disappears, which further confirms the transition between Ni^{2+} to Ni^{3+}.[48] Thus, the redox mechanism of NiCo LDH-based electrode during the charging process can be summarized as below:

$$Ni_{1-x}Co_x(OH)_2 + OH^- \leftrightarrow 1\text{-}x \cdot NiOOH + x \cdot CoOOH + H_2O + e^-$$

Furthermore, we investigated the reaction kinetics of the developed LDH-based alkaline zinc battery. As suggested by the CV curves with increased scanning rates from 2 to 8 mV s^{-1} (Figure 5d), the electrochemical polarization is weak in terms of peak shift, demonstrating the fast redox kinetics of LDH-based cathode during the electrochemical process. The linear fit of the relationship between logarithm (log) peak current and log scan rate (Figure 5e) shows that the slopes of cathodic and anodic peaks are 0.54 and 0.52, respectively, revealing the reaction mainly rely on the diffusion control rather than capacitive control.[49] In addition, we also investigated the ion transportation kinetics of the electrodes developed using the galvanostatic intermittent titration technique (GITT) tests.[50] Figure 5f and g

show the voltage response of NiCo LDH-based cathodes in GITT measurements. A long discharge plateau can be observed in both the LDH@NF battery and M–LDH@MXene/NF battery. In addition, we calculated the ion diffusion coefficient of the two electrodes, which are $1.1\times10^{-10}\,cm^2\,s^{-1}$ (LDH@NF) and $4.8\times10^{-8}\,cm^2\,s^{-1}$ (M–LDH@MXene/NF), respectively. The high ion diffusion coefficient of the MXene-supported LDH-based electrode further confirms the superiority of the electrodeposition method in the preparation of high-performance NiCo LDH electrode.[51]

Practicability of NiCo LDH Based Alkaline Zinc Battery

To verify the potential of NiCo LDH-based electrodes for practical application, a large-scale pouch cell with the size of 10×10 cm was assembled. As shown in Figure S12, stable discharge behavior can be achieved in the pouch cell with a 1.45 V average discharge voltage and up to ~1160 mAh discharge capacity, indicating the potential of the ZnO||M–LDH@MXene/NF battery as a practical energy storage device. It is worth noting that the rapid capacity decay could be observed in the initial cycles of the alkaline LDH-based batteries, which can be attributed to the partial decomposition of the electrolyte during initial cycles, the structural changes of the electrodes and some irreversible side reactions like corrosion and passivation in the electrode materials during initial cycles.[4] Furthermore, benefiting from the high electrodeposition loading of NiCo LDH active materials and excellent electrochemical activity of the M–LDH@MXene/NF cathode, remarkable areal energies and power densities ($16.3\,mWh\,cm^{-2}$ at $84.1\,mW\,cm^{-2}$) is achieved in the ZnO||M–LDH@MXene/NF pouch cell, which is superior to other pouch cell-level alkaline batteries (Figure S13).[17,45,46,52,53] In addition, we also calculated the volumetric energy density based on the anode and cathode, and up to $201\,Wh\,L^{-1}$ can be achieved in the alkaline NiCo LDH-based pouch cell. Moreover, the as-fabricated alkaline battery can undergo long-term cycling with high Coulombic efficiency and ~790 mAh discharge capacity can be maintained after 100 cycles, which confirms the decent stability and practicability of MXene-supported NiCo LDH-based cathode (Figure S14).

Conclusion

To improve the low energy density and poor cycling stability of aqueous rechargeable Ni||Zn batteries, we selected NiCo LDH as the potential cathode material and modified the electrodeposition preparation method based on the functional additive MXene. The resulting NiCo LDH-based electrode with remarkably boosted areal loading mass (~$65\,mg\,cm^{-2}$) and porous structure is readily obtained. The as-fabricated ZnO||M–LDH@MXene/NF battery presents ultrahigh capacity ($20.2\,mAh\,cm^{-2}$ or $311\,mAh\,g^{-1}$) and excellent cycling durability (88.6% after 10000 cycles). Moreover, this aqueous rechargeable alkaline zinc battery achieves an impressive energy density of $31.2\,mWh\,cm^{-2}$ ($465\,Wh\,Kg^{-1}$) and a peak power density of $80\,mW\,cm^{-2}$ ($2752\,W\,Kg^{-1}$), outperforming most reported aqueous rechargeable energy-storage devices. These findings may provide valuable insights into designing large-scale and high-performance electrodes for rechargeable AZBs.

Acknowledgements

This research was supported by the General Research Fund of the University Grants Committee under Project CityU 11212920.

Conflict of Interest

The authors declare no conflict of interest.

Data Availability Statement

The data that support the findings of this study are available from the corresponding author upon reasonable request.

Keywords: alkaline zinc batteries · layered double hydroxides · electrodeposition · MXene · aqueous batteries

[1] L. Ma, M. A. Schroeder, O. Borodin, T. P. Pollard, M. S. Ding, C. Wang, K. Xu, *Nat. Energy* **2020**, *5*, 743–749.
[2] C. Liu, X. Xie, B. Lu, J. Zhou, S. Liang, *ACS Energy Lett.* **2021**, DOI: 10.1021/acsenergylett.0c02684, 1015–1033.
[3] J. Shin, J. Lee, Y. Park, J. W. Choi, *Chem. Sci.* **2020**, *11*, 2028–2044.
[4] W. Shang, W. Yu, Y. Liu, R. Li, Y. Dai, C. Cheng, P. Tan, M. Ni, *Energy Storage Mater.* **2020**, *31*, 44–57.
[5] D. H. Wang, L. F. Wang, G. J. Liang, H. F. Li, Z. X. Liu, Z. J. Tang, J. B. Liang, C. Y. Zhi, *ACS Nano* **2019**, *13*, 10643–10652.
[6] X. L. Li, L. T. Ma, Y. W. Zhao, Q. Yang, D. H. Wang, Z. D. Huang, G. J. Liang, F. N. Mo, Z. X. Liu, C. Y. Zhi, *Mater. Today* **2019**, *14*, 100361.
[7] J. Ming, J. Guo, C. Xia, W. Wang, H. N. Alshareef, *Mater. Sci. Eng. R* **2019**, *135*, 58–84.
[8] H. F. Li, L. T. Ma, C. P. Han, Z. F. Wang, Z. X. Liu, Z. J. Tang, C. Y. Zhi, *Journal* **2019**, *62*, 550–587.
[9] Q. Zhao, W. Huang, Z. Luo, L. Liu, Y. Lu, Y. Li, L. Li, J. Hu, H. Ma, J. Chen, *Sci. Adv.* **2018**, *4*, eaao1761.
[10] W. Xu, Y. Wang, *Nano-Micro Lett.* **2019**, *11*, 90.
[11] G. Fang, J. Zhou, A. Pan, S. Liang, *ACS Energy Lett.* **2018**, *3*, 2480–2501.
[12] M. Li, J. Meng, Q. Li, M. Huang, X. Liu, K. A. Owusu, Z. Liu, L. Mai, *Adv. Funct. Mater.* **2018**, *28*, 1802016.
[13] H. Chen, Z. Shen, Z. Pan, Z. Kou, X. Liu, H. Zhang, Q. Gu, C. Guan, J. Wang, *Adv. Sci.* **2019**, *6*, 1802002.
[14] Y. Huang, W. S. Ip, Y. Y. Lau, J. Sun, J. Zeng, N. S. S. Yeung, W. S. Ng, H. Li, Z. Pei, Q. Xue, Y. Wang, J. Yu, H. Hu, C. Zhi, *ACS Nano* **2017**, *11*, 8953–8961.
[15] Y. Zeng, Y. Meng, Z. Lai, X. Zhang, M. Yu, P. Fang, M. Wu, Y. Tong, X. Lu, *Adv. Mater.* **2017**, *29*, 1702698.
[16] W. Zhou, D. Zhu, J. He, J. Li, H. Chen, Y. Chen, D. Chao, *Energy Environ. Sci.* **2020**, *13*, 4157–4167.

[17] W. He, S. Wang, Y. Shao, Z. Kong, H. Tu, Y. Wu, X. Hao, *Adv. Energy Mater.* **2021**, *11*, 2003268.
[18] H. Li, L. Ma, C. Han, Z. Wang, Z. Liu, Z. Tang, C. Zhi, *Nano Energy* **2019**, *62*, 550–587.
[19] M. Huang, M. Li, C. Niu, Q. Li, L. Mai, *Adv. Funct. Mater.* **2019**, *29*, 1807847.
[20] Z. Lu, X. Wu, X. Lei, Y. Li, X. Sun, *Inorg. Chem. Front.* **2015**, *2*, 184–187.
[21] R. Wang, Y. Han, Z. Wang, J. Jiang, Y. Tong, X. Lu, *Adv. Funct. Mater.* **2018**, *28*, 1802157.
[22] Y. Zeng, Z. Lai, Y. Han, H. Zhang, S. Xie, X. Lu, *Adv. Mater.* **2018**, *30*, 1802396.
[23] S. Wang, S. Lai, P. Li, T. Gao, K. Sun, X. Ding, T. Xie, C. Wu, X. Li, Y. Kuang, W. Liu, W. Yang, X. Sun, *J. Power Sources* **2019**, *436*, 226867.
[24] H.-J. Kang, G. A. R. Bari, T.-G. Lee, T. T. Khan, J.-W. Park, H. J. Hwang, S. Y. Cho, Y.-S. Jun, *Nanomaterials* **2020**, *10*, 2012.
[25] A. G. Slater, A. I. Cooper, *Science* **2015**, *348*, aaa8075.
[26] M. Li, J. Lu, Z. Chen, K. Amine, *Adv. Mater.* **2018**, *30*, 1800561.
[27] V. Mathew, N. B. Schorr, B. Sambandam, T. N. Lambert, J. Kim, *Accounts of Materials Research* **2023**, *4*, 299–306.
[28] C. Forano, T. Hibino, F. Leroux, C. Taviot-Guého, *Developments in clay science* **2006**, *1*, 1021–1095.
[29] P. Nalawade, B. Aware, V. Kadam, R. Hirlekar, **2009**.
[30] Y. Sun, C. Liu, L. Zhang, P. Wan, S. Zhuang, Y. Tang, Y. Chen, J. Pan, *ChemElectroChem* **2017**, *4*, 1044–1050.
[31] X. Lu, C. Zhao, *Nat. Commun.* **2015**, *6*, 6616.
[32] Z. Chen, X. Li, D. Wang, Q. Yang, L. Ma, Z. Huang, G. Liang, A. Chen, Y. Guo, B. Dong, X. Huang, C. Yang, C. Zhi, *Energy Environ. Sci.* **2021**, *14*, 3492–3501.
[33] Z. Chen, X. Ma, Y. Hou, H. Cui, X. Li, Q. Yang, Z. Huang, D. Wang, B. Dong, J. Fan, C. Zhi, *Adv. Funct. Mater.* **2022**, 2214539.
[34] G. R. Williams, D. O'Hare, *J. Mater. Chem.* **2006**, *16*, 3065–3074.
[35] F. Liu, E. Wang, C. Wu, D. Sun, J. Li, *J. Solid State Electrochem.* **2021**, *25*, 2033–2039.
[36] C. Zhang, J. Zhao, L. Zhou, Z. Li, M. Shao, M. Wei, *J. Mater. Chem. A* **2016**, *4*, 11516–11523.
[37] L. Hu, M. Li, X. Wei, H. Wang, Y. Wu, J. Wen, W. Gu, C. Zhu, *Chem. Eng. J.* **2020**, *398*, 125605.
[38] X. Li, Z. Huang, C. E. Shuck, G. Liang, Y. Gogotsi, C. Zhi, *Nat. Chem. Rev.* **2022**, *6*, 389–404.
[39] D. Wang, Y. Zhao, G. Liang, F. Mo, H. Li, Z. Huang, X. Li, T. Tang, B. Dong, C. Zhi, *Nano Energy* **2020**, *71*, 104583.
[40] W. Xie, K. Zhu, H. Yang, W. Jiang, W. Li, Z. Wang, W. Yang, *Angew. Chem. Int. Ed.* **2023**, *62*, e202303517.
[41] J. Tian, M. Peng, M. Luo, J. Lan, Y. Zhang, Y. Tan, *Small* **2022**, *18*, 2200452.
[42] T. Chen, F. Wang, S. Cao, Y. Bai, S. Zheng, W. Li, S. Zhang, S.-X. Hu, H. Pang, *Adv. Mater.* **2022**, *34*, 2201779.
[43] Y. Zhou, X. Tong, N. Pang, Y. Deng, C. Yan, D. Wu, S. Xu, D. Xiong, L. Wang, P. K. Chu, *ACS Appl. Mater. Interfaces* **2021**, *13*, 34292–34300.
[44] W. Zhou, J. He, D. Zhu, J. Li, Y. Chen, *ACS Appl. Mater. Interfaces* **2020**, *12*, 34931–34940.
[45] Z. Cui, S. Shen, J. Yu, J. Si, D. Cai, Q. Wang, *Chem. Eng. J.* **2021**, *426*, 130068.
[46] T. Chen, Y. Bai, X. Xiao, H. Pang, *Chem. Eng. J.* **2021**, *413*, 127523.
[47] H. Xu, J. Wu, J. Liu, Y. Chen, X. Fan, *J. Mater. Sci. Mater. Electron.* **2018**, *29*, 17234–17244.
[48] X. Wan, Y. Song, H. Zhou, M. Shao, *Energy Material Advances* **2022**, *2022*.
[49] Z. Chen, Q. Yang, F. Mo, N. Li, G. Liang, X. Li, Z. Huang, D. Wang, W. Huang, J. Fan, *Adv. Mater.* **2020**, 2001469.
[50] Z. Chen, C. Li, Q. Yang, D. Wang, X. Li, Z. Huang, G. Liang, A. Chen, C. Zhi, *Adv. Mater.* **2021**, 2105426.
[51] J. Fan, Q. Xiao, Y. Fang, L. Li, W. Yuan, *Ionics* **2019**, *25*, 1303–1313.
[52] R. Kumar, J. Shin, L. Yin, J.-M. You, Y. S. Meng, J. Wang, *Adv. Energy Mater.* **2017**, *7*, 1602096.
[53] A. Meng, T. Shen, G. Song, T. Huang, Y. Lin, H. Xue, X. Yuan, J. Zhao, Z. Li, *Mater. Charact.* **2020**, *165*, 110375.

Manuscript received: June 18, 2024
Accepted manuscript online: July 21, 2024
Version of record online: September 13, 2024